Fluid–structure interaction modeling of blood flow and cerebral aneurysm: Significance of artery and aneurysm shapes

Ryo Torii [a],*

[a]*Department of Chemical Engineering, Imperial College London, South Kensington Campus, London SW7 2AZ, United Kingdom* [a]

Marie Oshima [b]

[b]*Institute of Industrial Science, The University of Tokyo, 4-6-1 Komaba, Meguro, Tokyo, 153-8505, Japan*

Toshio Kobayashi [c]

[c]*Japan Automobile Research Institute, 2530 Karima, Tsukuba, Ibaraki 305-0822, Japan*

Kiyoshi Takagi [b,d]

[d]*Department of Neurosurgery, Fujita Health University, 1-98 Dengakugakubo, Kutsukake, Toyoake, Aichi 470-1192, Japan*

Tayfun E. Tezduyar [e]

[e]*Mechanical Engineering, Rice University – MS 321, 6100 Main Street, Houston, 77005 TX, USA*

Abstract

Because wall shear stress (WSS) is known to play an important role in initiation, growth and rupture of cerebral aneurysm, predicting the hemodynamic forces near the aneurysmal site helps with understanding aneurysms better. Earlier research reports indicate that the WSS around the aneurysmal site has a significant relationship with the vascular and aneurysm morphology. It was also shown statistically that the aneurysm shape (aspect ratio) is an indicator of rupture risk in cerebral aneurysm. In this study, fluid–structure interaction (FSI) modeling of a ruptured aneurysm, two unruptured aneurysms at the middle cerebral artery (MCA) bifurcation, and a MCA bifurcation without aneurysm is carried out using vascular geometries reconstructed from CT images. We use pulsatile boundary conditions based on a physiological flow velocity waveform and investigate the relationship between the

hemodynamic forces and vascular morphology for different arteries and aneurysms. The results are compared with the results obtained for the rigid arterial wall to highlight the role of FSI in the patient-specific modeling of cerebral aneurysm. The results show that the interaction between the blood flow and arterial deformation alters the hemodynamic forces acting on the arterial wall and the interaction strongly depends on the individual aneurysm shapes. Flow impingement on the arterial wall plays a key role in determining the interaction and hemodynamic forces. When the blood flow impinges strongly on the wall, the maximum WSS tends to decrease due to the flow–wall interaction. When the blood flows straight into an aneurysm, the flow and the resulting WSS patterns are altered both qualitatively and quantitatively. When the blood in the aneurysm is nearly stagnant, a slow flow is induced by the wall motion, which raises the minimum WSS on the aneurysmal wall. The results reinforce the importance of FSI in patient-specific analysis of cerebral aneurysms.

1 Introduction

Rupture of cerebral aneurysm is the leading cause of subarachnoid hemorrhage [1], one of the fatal diseases occurring in the human cerebral circulation. Cerebral aneurysm is linked to hemodynamics in the cerebral arterial network [2]. In particular, the wall shear stress (WSS) plays an important role in the disease progression of aneurysm because the arterial wall remodeling is controlled by the WSS acting on the endothelium [3]. The relationship between the blood flow, resulting WSS in the aneurysmal site and vascular morphology has been investigated from various aspects. From epidemiological point of view, aneurysm geometry characterized by the height, diameter, and neck width (or aspect ratio, AR = height/neck width, cf. Fig. 1) is reported statistically to indicate the progression and rupture risk of aneurysms [4,5]. Ujiie et al. [4] particularly connected the aneurysm progression to blood-flow stagnation owing to the aneurysm geometry. Detailed hemodynamics in cerebral aneurysms has been investigated experimentally [6] and computationally [7–11] to understand better the mechanisms contributing to the aneurysm progression. However, the mechanisms causing aneurysm still remain to be unveiled. One of the main findings regarding aneurysm hemodynamics so far is the sensitivity of the blood flow to the vascular morphology. Aspect ratio of an aneurysm [9], ratio of the aneurysm size to parent vessel diameter [12] and

* Corresponding author, Tel: +44 (0)20 7589 5111 ext. 55620
  Email address: `r.torii@imperial.ac.uk` (Ryo Torii).

the way an aneurysm is connected to the parent vessel (e.g. angle, curvature and tortuosity of the parent vessel) [10] are important factors determining hemodynamics in an aneurysm. In addition, using fluid–structure interaction (FSI) analysis, we reported earlier in [11] that the dynamic change in vascular morphology and hypertensive blood pressure, which is one of the risk factors in subarachnoid hemorrhage, affects the hemodynamics. However, the importance of FSI in cerebral aneurysms is still debated because the human intracranial arteries are stiffer than the other arteries [13], and it was asserted in an earlier computational–angiographical study that the impact of vascular motion on the hemodynamics is not crucial [10].

In this paper, FSI modeling of three aneurysms at Y-shaped bifurcations and a bifurcated artery without aneurysm are carried out. To gain a clearer view on the roles of FSI in various type of cerebral aneurysms, the results are compared to those obtained for the rigid arterial wall for the same subjects. The authors investigated in [14] the role of FSI in aneurysms, including two subjects with hypertensive blood pressure. This study expands the range of geometric variation to four subjects, but under normotensive blood pressure, to broaden our understandings. In particular, inclusion of a bifurcation without aneurysm would enable us to evaluate the role of FSI in aneurysms at initial stages. Since FSI modeling in arterial fluid mechanics is becoming more common [14–18], it is worth elucidating the importance of FSI in this class of problem with a wider range of aneurysms.

2 Computational method

The blood flow in cerebral arteries is assumed to be laminar [19] and governed by the Navier–Stokes equations of incompressible flows. The fluid mechanics with moving and deforming walls is computed with the Deforming-Spatial-Domain/Stabilized Space–Time (DSD/SST) method [20–23]. In the DSD/SST formulation, the streamline-upwind /Petrov-Galerkin (SUPG) [24,25] and pressure-stabilizing/Petrov-Galerkin (PSPG) [20,26] formulations are employed for stabilization. An earlier version of the pressure stabilization, for Stokes flows, was introduced in [27]. The DSD/SST method was introduced for flows with moving boundaries and interfaces and has been applied to a large class of problems [28–35], including FSI [36–42]. New versions of the DSD/SST method were introduced in [42] together with new versions of the space–time FSI technique.

The structural mechanics is governed by the force equilibrium equations and computed with the Galerkin finite element method. The arterial structure is modeled as linearly-elastic material with finite strain. Although arterial and aneurysmal walls are known to be governed by complicated constitutive

laws [43], it was shown in [44] by comparison between the linearly-elastic and hyper-elastic material models that the linearly-elastic material model would be able to represent the trends in displacement patterns.

The fluid and structural mechanics systems are coupled at the interface by kinematic and dynamic conditions. The two systems are solved with a block-iterative coupling approach [40,45]. The fluid mesh is updated by using an automatic mesh moving method [28,46], where the motion of the nodal points is governed by the equations of elasticity. The boundary conditions come from the motion of the interface between the fluid and structure. Details of the computational method are described in [15].
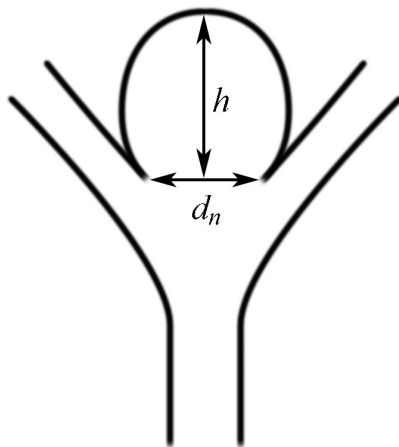

Fig. 1. Definition of aspect ratio, $AR = h/d_n$ (h and d_n are height and neck width of the aneurysm).

3   Computational model

Three aneurysm models at the middle cerebral artery (MCA) bifurcation and a MCA bifurcation with no aneurysm were reconstructed based on CT images. The models are shown in Figure 2. Subject 1 is a 59 year-old female; the aneurysm was ruptured before it was scanned. Subject 2 is a 67 year-old female; the aneurysm was unruptured. The aneurysm of Subject 3 was also unruptured but the age and gender are unknown. Subject 4 is a 51 year-old male.

Approximately 150 CT slices with 0.60 mm intervals were used for the geometry reconstruction. Each slice consists of 512×512 pixels. The in-plane resolution of a slice is 0.3125 mm/pixel. The surface of the arterial lumen was then constructed using the marching-cubes method [47] as an iso-surface at a certain CT signal intensity representing the arterial lumen. The reconstruction process was carried out with the commercial software ALATOVIEW (Toshiba
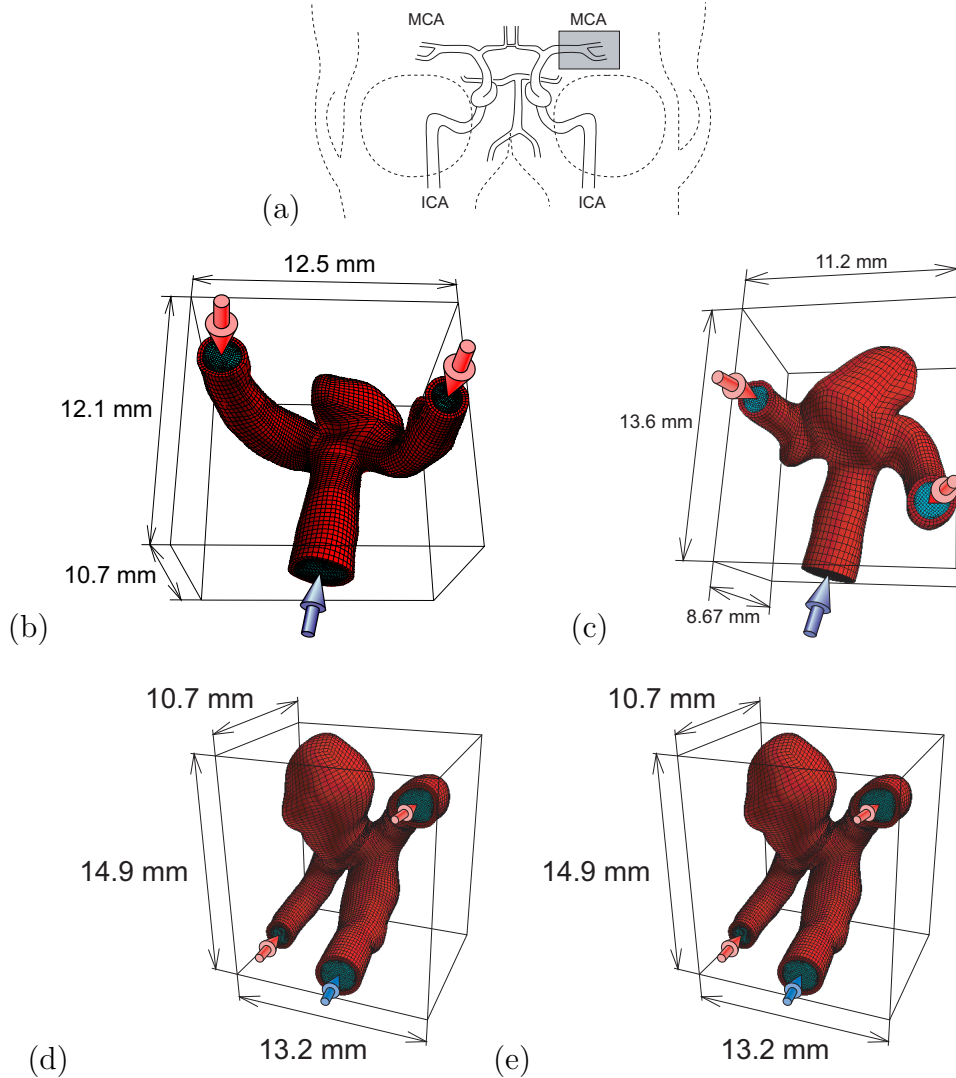
Fig. 2. Aneurysm models based on CT images. (a) Cerebral arterial network and the location of the middle cerebral artery (MCA). The internal carotid artery (ICA) provides the main blood supply to the cerebral arterial network, branching off of the common carotid artery. (b), (c) and (d) Aneurysm models for Subject 1 (59 year-old female, ruptured aneurysm), Subject 2 (67 year-old female, unruptured aneurysm) and Subject 3 (age and gender are unknown, unruptured aneurysm). (d) a MCA bifurcation model without aneurysm (Subject 4, 51 year-old male). The blue arrow denotes the inflow and the red arrows denote the resistance at the outlet from the peripheral arterial network.

medical, Inc.). Because the wall of the intracranial arteries is not thick enough to be resolved in CT images, it was added by assuming a uniform wall thickness of 0.3 mm (10% of the diameter [48]) and inflating the luminal wall outward. The arterial wall and the lumen for the four subjects are shown in red and blue in Figure 2. The diameter, height, neck width (= diameter at the open mouth of the aneurysm) and the resulting aspect ratio of the aneurysms, and the proximal/distal vessel diameters are summarized in Table 1. In Ujiie et

al. [4], aneurysm shape is classified by the reference aspect ratio 1.6. Subject 1 shows the typical geometric features of an unruptured aneurysm (< 1.6). On the other hand, the aspect ratio for Subject 2 is within the typical range of a ruptured aneurysm. The aspect ratio for Subject 3 is a borderline value.

Eight-noded hexahedral elements are used for the finite element discretization as shown in Figure 2. First-order interpolation functions are employed for all variables. The number of nodes and elements are summarized in Table 2. For fluid mechanics computations, the maximum element size in the axial (stream-wise), circumferential and cross-sectional directions are approximately 0.275, 0.164 and 0.228 mm, respectively. For structural mechanics part, the element size in the axial and circumferential directions are the same as those for fluid mechanics part, and the wall thickness is resolved with two layers of elements. These were determined based on a mesh sensitivity test comparing the results obtained with various mesh densities to determine how small the mesh sizes should be to obtain results that are independent of the mesh density. The simulations were carried out on HITACHI SR11000 at Information Technology Centre, The University of Tokyo. Computing one cardiac cycle took approximately three days with 16 CPUs.

Table 1
Geometric features of the aneurysms. Here d_{max}, d_n and h are the maximum diameter, neck width and height. Aspect ratio, $AR = h/d_n$. The diameter of the artery at the proximal and distal ends are denoted by d_{prox} and d_{dist}, respectively.

Subject	d_{max} [mm]	d_n [mm]	h [mm]	AR	d_{prox} [mm]	d_{dist} [mm]
1	5.64	3.99	2.93	0.73	2.74	1.51 / 2.01
2	4.90	2.57	7.22	2.81	2.38	1.75 / 1.51
3	6.35	4.02	6.54	1.63	2.49	1.64 / 2.09
4	–	–	–	–	3.33	1.99 / 1.91

Table 2
Number of nodes (N_n) and elements (N_e) used in the computations. Here the superscripts f and s denote the fluid and structure.

Subject	N_n^f	N_e^f	N_n^s	N_e^s
1	49,395	45,760	11,520	10,800
2	53,769	50,240	17,397	11,480
3	81,991	76,896	25,701	16,992
4	50,287	47,072	15,789	10,432

4 Mechanical properties and boundary conditions

Although the blood is known to be non-Newtonian in general, we assume it to be Newtonian in this study. We are focusing on arteries with diameters and flow rates in the range of 3.0 mm and 2.0 ml/s, respectively. Hence the averaged shear rate in the arteries is approximately $\dot{\gamma} = 4Q/(\pi R_0^3) \sim 755$ s^{-1} (Q and R_0 are flow rate and radius). The viscosity of the blood can be approximated as a constant when the shear rate in the flow is high enough (> 150 s^{-1}) [49]. Cebral, et al. show in [50] that for cerebral aneurysms treatment of blood as Newtonian does not alter the computational results compared to treating it as non-Newtonian. The density and viscosity of the blood are set to 1,000 kg/m^3 and 4.0×10^{-3} Pa·s, respectively. The arterial wall is assumed to be made of linearly-elastic material. Its density is 1,000 kg/m^3. The elastic modulus and Poisson's ratio are set to 1.0 MPa and 0.49 based on a computational pressure–radius relationship test [15] and experimental results [13].

The inflow boundary conditions are specified as a pulsatile velocity profile prescribed by Womersley's solution of a pulsatile flow in a rigid straight pipe [51]. The coefficients representing physiological waveform were determined based on the waveform acquired with ultrasound Doppler at the carotid artery of a healthy volunteer in his 20's. Figure 3 shows the flow waveform based on the measured velocity, with the velocity profile modeled by the Womersley's formulation.

Pressure conditions representing the resistance due to the peripheral arterial network are modeled by the normal stress at the boundaries, which are shown with red arrows in Fig. 2. The time-dependent pressure is obtained with the expression

$$P = P_0 + QR, \tag{1}$$

where Q is the total outflow. Here P_0 is a reference pressure and R represents the resistance owing to the distal vascular tree, which were determined to obtain physiological pressure range, 80–120 mm Hg (10,640–15,960 Pa). The pressure waveform is shown in Fig. 3. At the interface between the blood and the arterial wall, no-slip conditions are applied in the fluid mechanics part and hemodynamic forces in the structural mechanics part. Only the difference of the hemodynamic force from the level at the beginning of the cardiac cycle is applied to the arterial wall. The boundary displacements at the inlet and two outlets of the artery are set to zero. Influence of the residual stress is not taken into account.
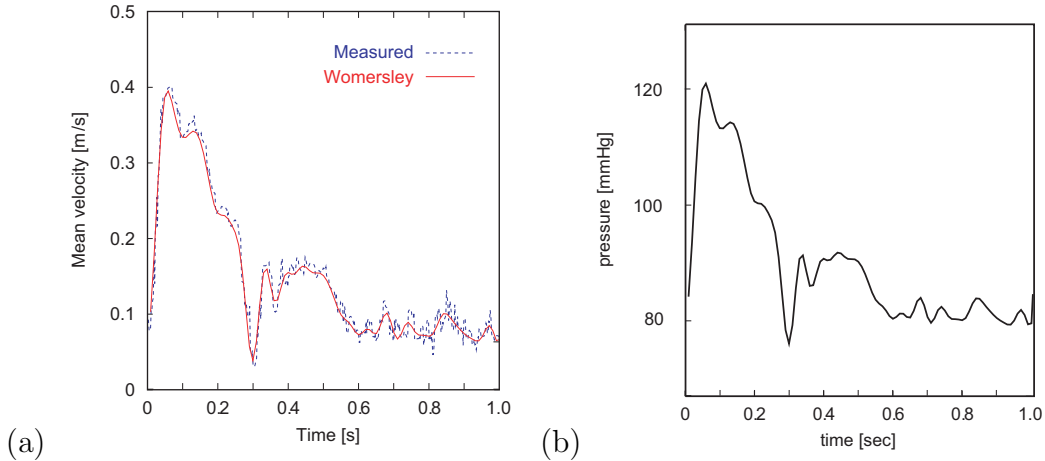
Fig. 3. Spatial mean velocity (a) and pressure (b) waveforms. The flow waveform is based on the velocity measured at the common carotid artery with ultrasound Doppler velocimeter. The pressure waveform is determined based on the flow waveform to obtain the physiological range of pressure assuming that there is no phase lag.

5 Results and discussion

5.1 Arterial and aneurysm wall deformation

Figure 4 shows the displacement patterns for the four subjects. The displacement is evident near the bifurcation for all cases. The maximum displacement is 0.652, 0.346, 0.623 and 0.316 mm for Subjects 1–4, respectively. They occur at the peak systole in all cases. The maximum displacement is in the order of one tenth of the arterial diameter $\sim$2–3 mm (cf. Tab. 1). The artery and aneurysm wall dilate because of the blood pressure. For Subjects 1 and 2, the displacement profiles show widening pattern whereas for Subject 3, the pattern indicates elongation where the displacement is the maximum at the apex and gradually decreases toward the neck.

5.2 Wall shear stress

The most interesting hemodynamic parameter in relation to the aneurysm progression is the WSS. It varies in time due to the pulsatility of the flow waveform (cf. Fig. 3) and the maximum value generally occurs at the peak systole when the inflow becomes the maximum. Figure 5 shows the WSS profiles at the peak systole for all cases. The maximum WSS at the peak systole, which is indicated with a white circle in the figure, is 428, 430, 326 and 382 dyn/cm^2 for Subjects 1–4 for the rigid arterial wall. On the other hand,
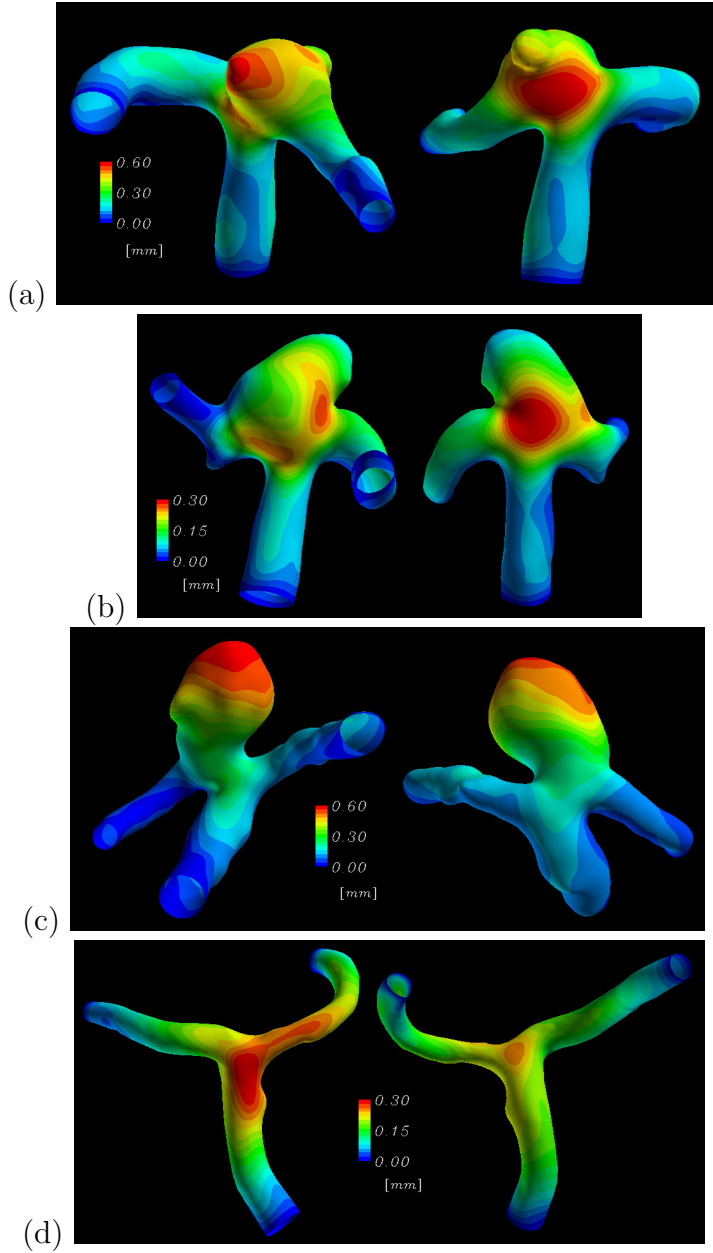
Fig. 4. Displacement patterns for Subjects 1–4 (a–d, respectively).

the maximum WSS at the peak systole for the compliant arterial wall is 329, 345, 344 and 381 dyn/cm² for Subjects 1–4. As previously reported [11,14], the WSS profile for the compliant arterial wall is altered from that for the rigid wall by the interaction between the blood flow and arterial wall deformation. For example, the WSS for the rigid wall model is approximately 20% larger than that for the compliant wall model for Subjects 1 and 2, although nearly the same for Subjects 3 and 4. The WSS on the aneurysmal wall, playing an important role in the progression of aneurysm, follows the same trend as the above-mentioned maximum WSS. For Subject 1, the maximum WSS occurs on the aneurysmal wall. For Subject 2, the maximum WSS on the aneurysmal

wall is 177 and 119 dyn/cm^2 for the rigid and compliant wall cases. The WSS on the aneurysmal wall for Subject 3 is very small for the two wall models, less than 10 dyn/cm^2. It was reported that 10 dyn/cm^2 is the lower limit of physiological WSS range [52] and WSS lower than 4 dyn/cm^2 causes atherosclerotic change in arterial wall [52]. Hence the WSS level observed here is potentially pro-pathological condition.

The flow–wall interaction also alters quantitatively the WSS profile on the aneurysm. The WSS after the peak systole (t= 0.10 s) for the rigid wall (Fig. 6 (a)) shows focal high value on the wall and the WSS is very low ($\sim$ 10 dyn/cm^2) near the apex. On the other hand, the WSS near the apex for the compliant wall is much higher ($\sim$ 40 dyn/cm^2). Low WSS occurring near the apex is known to play a role in rupture of aneurysm via degradation of the aneurysmal wall [4] because very low WSS results in abnormal metabolic activity in arterial wall [2,52]. Considering this, flow–wall interaction induces more pathological state for Subject 1 in terms of the WSS where the area of low WSS is spread wider but it works more protective to the aneurysm for Subject 2 by preventing a rupture-prone hemodynamic pattern. The WSS pattern is altered by the wall motion in Subject 3 as well (cf. Fig. 6 (b)). The WSS on the aneurysm wall is very small, close to zero (within the first contour level, $<$ 2 dyn/cm^2), for the rigid arterial wall whereas the WSS profile for the compliant wall exhibits higher value (up to the third contour level, $\sim$ 6 dyn/cm^2) although both of them are still lower than the physiologically normal range ($>$ 10 dyn/cm^2). However, since a WSS value lower than 4 dyn/cm^2 is considered to be pro-pathological condition, this small difference in the WSS could play a significant role in disease progression.

5.3 Interaction between the blood flow and wall deformation

The velocity profiles shown in Figs. 7 and 8 depict the effect of the wall deformation on the WSS profiles since the interaction between the blood flow and arterial wall dynamics is reflected to the WSS through the velocity profile. The flows in bifurcated vessels tend to impinge on the arterial wall near the branching point; for example in Subject 1, the flow from the inlet proceeds in the parent artery and impinges on the wall at the neck of the aneurysm. All flow impingements are indicated by a yellow triangular arrow in Fig. 7. The hemodynamics around the region where the blood flow impinges on the wall is highly susceptible to wall deformation. The wall dilation in the systole owing to increasing pressure makes the wall moving away from the flow impingement, resulting in smaller impact and consequently lower WSS. This is typically observed in Subject 1. In addition, the impinging flow velocity near the neck of the aneurysm is smaller for the compliant wall case than for the rigid wall case (cf. Fig. 7 (a)) because of the dilatation of the parent vessel leading to the

smaller velocity in the axial direction. The same trend is seen in Subjects 2 and 4 as well; the focal high WSS observed in the rigid wall case (on the aneurysmal wall in Subject 2 and on the right branch in Subject 4 in Fig. 5) is weakened in the compliant wall case because of the above-mentioned flow–wall interaction mechanism. However, the difference in velocity profiles at the peak systole for the rigid and compliant walls for Subjects 3 is much smaller than those for the other subjects. This is because the majority of the flow in Subject 3 proceeds to the right branch in Fig. 7 and does not impinge strongly on the wall in the branching region. The WSS in the impingement region (cf. Fig. 5) is only slightly higher than the other part. It is also notable that the blood flow does not enter the aneurysm for this subject. Hence the WSS on the aneurysm is very low independent of the flow–wall interaction. This indicates that in terms of high WSS, the FSI is insignificant for Subject 3 compared to Subjects 1, 2 and 4.

The qualitative difference in the WSS profiles observed for Subjects 2 and 3 can also be explained via the velocity profiles. Figure 8 shows the velocity profiles corresponding to the WSS profiles in Fig. 6. Although the velocity profiles at the peak systole for Subject 2 are similar between the rigid and elastic wall cases, those after the peak are significantly different. In the rigid wall case, there is a large vortex accompanied by a smaller vortex near the apex whilst a single vortex is observed in the compliant wall case. The difference in the flow patterns owing to the displacement of the arterial wall is indicated by a white triangular marker in Fig. 8 (a). In the original aneurysm shape, the wall is curved and bends the flow toward the other side of the wall, making it impinge on the wall. The flow forms twin vortices after the impingement. The twin-vortex flow pattern persists after the peak systole when the flow–wall interaction is not considered. However, the flow proceeds straight along the wall, which was inflated by the blood pressure, towards the apex when the wall is compliant. The secondary vortex consequently diminishes. Since this secondary vortex is viewed as causing the aneurysm to rupture [4], the difference in the flow patterns can be significant. The velocity profiles for Subject 3 shown in Fig. 8 (b) also exhibit differences. The blood in the aneurysm is nearly stagnant (within the first contour level, $< 6.25 \times 10^{-3}$ m/s), especially near the apex when the wall is modeled as rigid, whereas the velocity magnitude rises to approximately 0.025 m/s in the compliant wall case. The flow in the compliant wall case is induced by the wall motion that elongates the aneurysm toward the apex (cf. Fig. 4), resulting in higher WSS on the aneurysmal wall than in the rigid wall case. The WSS for the compliant wall case is indeed higher than the range considered pathological (< 4 dyn/cm^2), and the hemodynamic condition in the aneurysm is potentially protective to disease progression due to the flow–wall interaction. Hence the flow–wall interaction could play an important role for Subject 3 in terms of low WSS. Quantitative evaluation of the WSS is still difficult because there are other factors influencing the level of the WSS, such as inflow velocity, wall thickness and elasticity.

However, the results shed additional light on the importance of fluid–structure interaction in patient-specific computation of cerebral aneurysms.

6   Conclusions

Patient-specific fluid–structure interaction (FSI) analyses were carried out for one ruptured cerebral aneurysm, two unruptured aneurysm, and a Y-shaped bifurcation without aneurysm, all at the middle cerebral artery and reconstructed based on CT images. The results were compared with the results for the rigid arterial walls to broaden the previously acquired knowledge [14] on the importance of FSI in patient-specific simulations of cerebral aneurysms. The results show that the role of FSI depends on the shape of the aneurysm, particularly on the region of flow impingement and the displacement pattern in individual arterial geometry. For the cases where the blood flow impinges strongly on the wall, the maximum WSS tends to decrease with the FSI. When the blood flows straight into an aneurysm, the flow and the resulting WSS patterns are altered by the flow–wall interaction both qualitatively and quantitatively. If the flow does not enter an aneurysm and the blood in the aneurysm is nearly stagnant, the effect of FSI appears insignificant but a slow flow is induced in the aneurysm by the wall motion that raises the minimum WSS on the aneurysmal wall. The results reinforce the importance of FSI in patient-specific analysis of cerebral aneurysms although the role of FSI appears differently in individual aneurysms, depending on the vascular geometry.

References

[1] J. van Gijn and G. J. E. Rinkel, "Subarachnoid heamorrhage: diagnosis, cause and management", *Brain*, **124** (2001) 249–278.

[2] H. J. Steiger, "Pathophysiology of development and rupture of cerebral aneurysms", *Acta Neurochirurgica Suppliment*, **48** (1990) 1–57.

[3] S. Lehoux, F. Tronc, and A. Tedgui, "Mechanisms of blood flow-induced vascular enlargement", *Biorheology*, **39** (2002) 319–324.

[4] H. Ujiie, H. Tachibana, O. Hiramatsu, A. Hazel, T. Matsumoto, Y. Ogasawara, H. Nakajima, T. Hori, K. Takakura, and F. Kajiya, "Effects of size and shape (aspect ratio) on the hemodynamics of saccular aneurysms: A possible index for surgical treatment of intracranial aneurysms", *Neurosurgery*, **45** (1999) 119–130.

[5] S. M. Russel, K. Lin, Sigrid, S. A. Hahn, and J. J. Jafar, "Smaller cerebral aneurysms producing more extensive subarachnoid hemorrhage following rupture: a radiological investigation and discussion of theoretical determinants", *Journal of Neurosurgery*, **99** (2003) 248–253.

[6] S. Tateshima, Y. Murayama, J. P. Villablanca, T. Morino, H. Takahashi, T. Yamauchi, K. Tanishita, and F. Vinuela, "Intraaneurysmal flow dynamics study featuring an acrylic aneurysm model manufactured using a computerized tomography angiogram as a mold", *Journal of Neurosurgery*, **95** (2001) 1020–1027.

[7] A. C. Burleson, C. M. Strother, and V. T. Turitto, "Computer modeling of intracranial saccular and lateral aneurysms for the study of theirhemodynamics", *Neurosurgery*, **37** (1995) 774–783.

[8] G. N. Foutrakis, H. Yonas, and R. J. Sclabassi, "Saccular aneurysm formation in curved and bifurcating arteries", *American Journal of Neuroradiology*, **20** (1999) 1309–1317.

[9] M. Shojima, M. Oshima, K. Takagi, R. Torii, M. Hayakawa, K. Katada, M. Morita, and T. Kirino, "Magnitude and role of wall shear stress on cerebral aneurysm: computational fluid dynamic study of 20 middle cerebral artery aneurysms", *Stroke*, **35** (2004) 2500–2505.

[10] J. R. Cebral, M. A. Castro, J. E. Burgess, R. S. Pergolizzi, M. J. Sheridan, and C. M. Putman, "Characterization of cerebral aneurysms for assessing risk of rupture by using patient-specific computational hemodynamics models", *American Journal of Neuroradiology*, **26** (2005) 2550–2559.

[11] R. Torii, M. Oshima, T. Kobayashi, K. Takagi, and T. E. Tezduyar, "Fluid–structure interaction modeling of aneurysmal conditions with high and normal blood pressures", *Computational Mechanics*, **38** (2006) 482–490.

[12] H. Zakaria, H. Yonas, and A. M. Robertson, "Analysis of the importance of the ratio of aneurysm size to parent artery diameter on hemodynamic condition", *Journal of Biomechanics*, **39** (2006) S272.

[13] K. Hayashi, H. Handa, S. Nagasawa, A. Okumura, and K. Moritake, "Stiffness and elastic behavior of human intracranial and extracranial arteries", *Journal of Biomechanics*, **13** (1980) 175–184.

[14] R. Torii, M. Oshima, T. Kobayashi, K. Takagi, and T. E. Tezduyar, "Numerical investigation of the effect of hypertensive blood pressure on cerebral aneurysm — Dependence of the effect on the aneurysm shape", *International Journal for Numerical Methods in Fluids*, **54** (2007) 995–1009.

[15] R. Torii, M. Oshima, T. Kobayashi, K. Takagi, and T. E. Tezduyar, "Computer modeling of cardiovascular fluid–structure interactions with the Deforming-Spatial-Domain/Stabilized Space–Time formulation", *Computer Methods in Applied Mechanics and Engineering*, **195** (2006) 1885–1895.

[16] Y. Bazilevs, V. M. Calo, Y. Zhang, and T. J. R. Hughes, "Isogeometric fluid–structure interaction analysis with applications to arterial blood flow", *Computational Mechanics*, **38** (2006) 310–322.

[17] T. E. Tezduyar, S. Sathe, T. Cragin, B. Nanna, B. S. Conklin, J. Pausewang, and M. Schwaab, "Modeling of fluid–structure interactions with the space–time finite elements: Arterial fluid mechanics", *International Journal for Numerical Methods in Fluids*, **54** (2007) 901–922.

[18] T. E. Tezduyar, S. Sathe, M. Schwaab, and B. S. Conklin, "Arterial fluid mechanics modeling with the stabilized space–time fluid–structure interaction technique", *International Journal for Numerical Methods in Fluids*, **57** (2008) 601–629.

[19] T. Karino, S. Takeuchi, N. Kobayashi, M. Motomiya, and S. Mabuchi, "Fluid dynamics of cerebrovascular disease (in Japanese)", *Neurosurgeons*, **12** (1993) 15–24.

[20] T. E. Tezduyar, "Stabilized finite element formulations for incompressible flow computations", *Advances in Applied Mechanics*, **28** (1992) 1–44.

[21] T. E. Tezduyar, M. Behr, and J. Liou, "A new strategy for finite element computations involving moving boundaries and interfaces – the deforming-spatial-domain/space–time procedure: I. The concept and the preliminary numerical tests", *Computer Methods in Applied Mechanics and Engineering*, **94** (1992) 339–351.

[22] T. E. Tezduyar, M. Behr, S. Mittal, and J. Liou, "A new strategy for finite element computations involving moving boundaries and interfaces – the deforming-spatial-domain/space–time procedure: II. Computation of free-surface flows, two-liquid flows, and flows with drifting cylinders", *Computer Methods in Applied Mechanics and Engineering*, **94** (1992) 353–371.

[23] T. E. Tezduyar, "Computation of moving boundaries and interfaces and stabilization parameters", *International Journal for Numerical Methods in Fluids*, **43** (2003) 555–575.

[24] T. J. R. Hughes and A. N. Brooks, "A multi-dimensional upwind scheme with no crosswind diffusion", in T. J. R. Hughes, editor, *Finite Element Methods for Convection Dominated Flows*, AMD-Vol.34, 19–35, ASME, New York, 1979.

[25] A. N. Brooks and T. J. R. Hughes, "Streamline upwind/Petrov-Galerkin formulations for convection dominated flows with particular emphasis on the incompressible Navier-Stokes equations", *Computer Methods in Applied Mechanics and Engineering*, **32** (1982) 199–259.

[26] T. E. Tezduyar, S. Mittal, S. E. Ray, and R. Shih, "Incompressible flow computations with stabilized bilinear and linear equal-order-interpolation velocity-pressure elements", *Computer Methods in Applied Mechanics and Engineering*, **95** (1992) 221–242.

[27] T. J. R. Hughes, L. P. Franca, and M. Balestra, "A new finite element formulation for computational fluid dynamics: V. Circumventing the Babuška–Brezzi condition: A stable Petrov–Galerkin formulation of the Stokes problem accommodating equal-order interpolations", *Computer Methods in Applied Mechanics and Engineering*, **59** (1986) 85–99.

[28] T. Tezduyar, S. Aliabadi, M. Behr, A. Johnson, and S. Mittal, "Parallel finite-element computation of 3D flows", *Computer*, **26** (1993) 27–36.

[29] T. E. Tezduyar, S. K. Aliabadi, M. Behr, and S. Mittal, "Massively parallel finite element simulation of compressible and incompressible flows", *Computer Methods in Applied Mechanics and Engineering*, **119** (1994) 157–177.

[30] T. Tezduyar, S. Aliabadi, M. Behr, A. Johnson, V. Kalro, and M. Litke, "Flow simulation and high performance computing", *Computational Mechanics*, **18** (1996) 397–412.

[31] T. E. Tezduyar, "CFD methods for three-dimensional computation of complex flow problems", *Journal of Wind Engineering and Industrial Aerodynamics*, **81** (1999) 97–116.

[32] T. E. Tezduyar, "Finite element methods for flow problems with moving boundaries and interfaces", *Archives of Computational Methods in Engineering*, **8** (2001) 83–130.

[33] T. E. Tezduyar, "Interface-tracking and interface-capturing techniques for finite element computation of moving boundaries and interfaces", *Computer Methods in Applied Mechanics and Engineering*, **195** (2006) 2983–3000.

[34] T. E. Tezduyar, "Finite elements in fluids: Stabilized formulations and moving boundaries and interfaces", *Computers & Fluids*, **36** (2007) 191–206.

[35] T. E. Tezduyar, "Finite elements in fluids: Special methods and enhanced solution techniques", *Computers & Fluids*, **36** (2007) 207–223.

[36] S. Mittal and T. E. Tezduyar, "Parallel finite element simulation of 3D incompressible flows – Fluid-structure interactions", *International Journal for Numerical Methods in Fluids*, **21** (1995) 933–953.

[37] V. Kalro and T. E. Tezduyar, "A parallel 3D computational method for fluid–structure interactions in parachute systems", *Computer Methods in Applied Mechanics and Engineering*, **190** (2000) 321–332.

[38] T. Tezduyar and Y. Osawa, "Fluid–structure interactions of a parachute crossing the far wake of an aircraft", *Computer Methods in Applied Mechanics and Engineering*, **191** (2001) 717–726.

[39] K. R. Stein, R. J. Benney, T. E. Tezduyar, J. W. Leonard, and M. L. Accorsi, "Fluid–structure interactions of a round parachute: Modeling and simulation techniques", *Journal of Aircraft*, **38** (2001) 800–808.

[40] T. E. Tezduyar, S. Sathe, R. Keedy, and K. Stein, "Space–time finite element techniques for computation of fluid–structure interactions", *Computer Methods in Applied Mechanics and Engineering*, **195** (2006) 2002–2027.

[41] T. E. Tezduyar, S. Sathe, and K. Stein, "Solution techniques for the fully-discretized equations in computation of fluid–structure interactions with the space–time formulations", *Computer Methods in Applied Mechanics and Engineering*, **195** (2006) 5743–5753.

[42] T. E. Tezduyar and S. Sathe, "Modeling of fluid–structure interactions with the space–time finite elements: Solution techniques", *International Journal for Numerical Methods in Fluids*, **54** (2007) 855–900.

[43] J. D. Humphrey, *Cardiovascular Solid Mechanics. Cells, Tissues, and Organs.* Springer-Verlag, New York, 2002.

[44] R. Torii, M. Oshima, T. Kobayashi, K. Takagi, and T. E. Tezduyar, "Fluid–structure interaction modeling of a patient-specific cerebral aneurysm: influence of structural modeling", *Computational Mechanics*, Accepted.

[45] T. E. Tezduyar, "Finite element methods for fluid dynamics with moving boundaries and interfaces", in E. Stein, R. De Borst, and T. J. R. Hughes, editors, *Encyclopedia of Computational Mechanics*, Volume 3: Fluids, Chapter 17, John Wiley & Sons, 2004.

[46] T. E. Tezduyar, M. Behr, S. Mittal, and A. A. Johnson, "Computation of unsteady incompressible flows with the finite element methods – space–time formulations, iterative strategies and massively parallel implementations", in *New Methods in Transient Analysis*, PVP-Vol.246/AMD-Vol.143, ASME, New York, (1992) 7–24.

[47] W. E. Loremson and H. E. Cline, "Marching Cubes: a high resolution 3D surface construction algorithm", *Computer Graphics*, **21** (1987) 163–169.

[48] W. A. Riley, R. W. Barnes, G. W. Evans, and G. L. Burke, "Ultrasonic measurement of the elastic modulus of the common carotid artery. The atherosclerosis risk in communities (ARIC) study", *Stroke*, **23** (1992) 952–956.

[49] R. E. Wells Jr. and E. W. Merrill, "Shear rate dependence of the viscosity of whole blood and plasma", *Science*, **133** (1961) 763–764.

[50] J. R. Cebral, M. A. Castro, S. Appanaboyina, C. M. Putman, D. Millan, and A. F. Frangi, "Efficient pipeline for image-based patient-specific analysis of cerebral aneurysm hemodynamics: technique and sensitivity", *IEEE Transactions on Medical Imaging*, **24** (2005) 457–467.

[51] J. R. Womersley, "Method for the calculation of velocity, rate of flow and viscous drag in arteries when the pressure gradient is known", *Journal of Physiology*, **127** (1955) 553–563.

[52] A. M. Malek, S. L. Alper, and S. Izumo, "Hemodynamic shear stress and its role in atherosclerosis", *The Journal of the American Medical Association*, **282** (1999) 2035–2042.
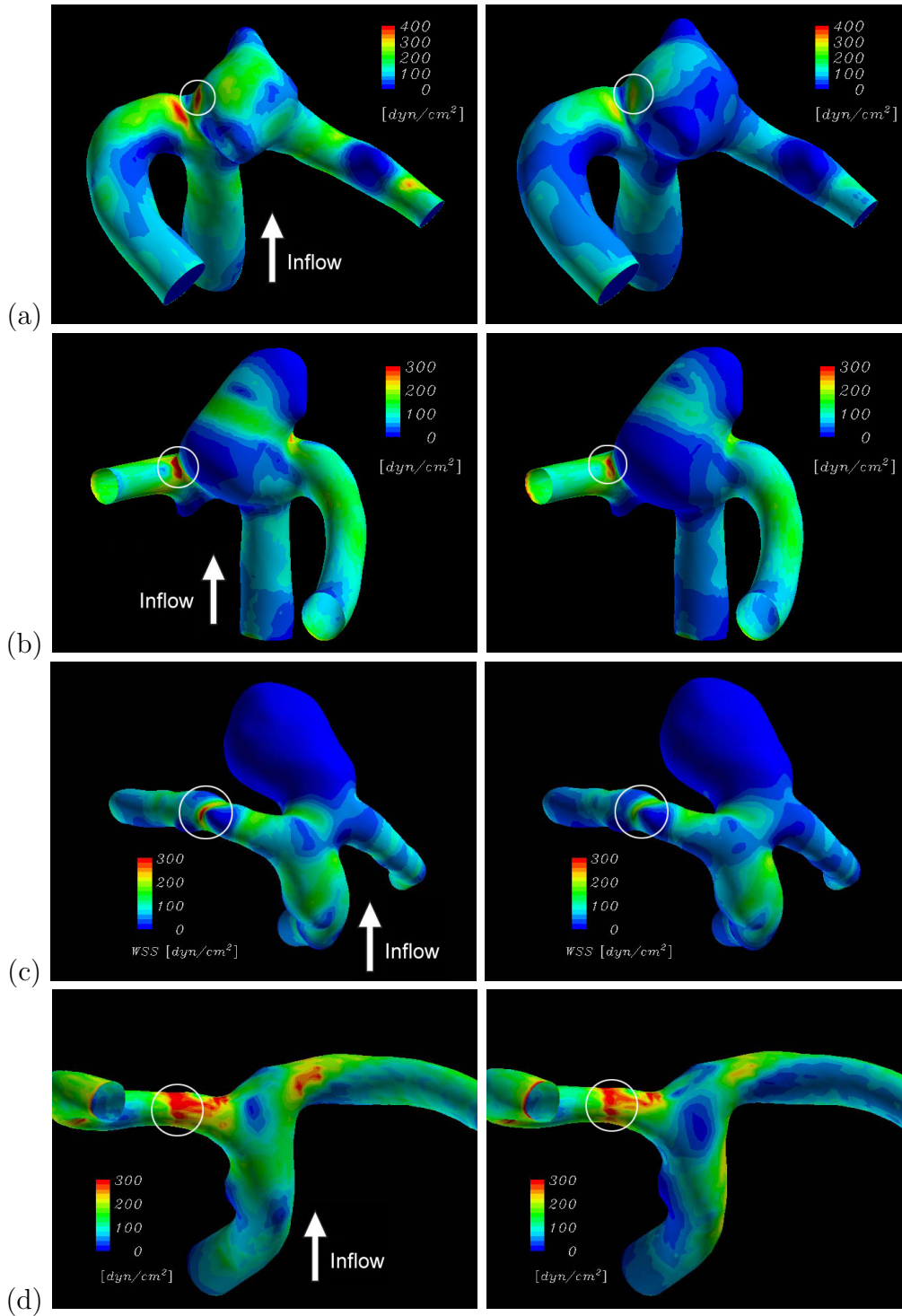
Fig. 5. Comparison of the WSS profiles at the peak systole for Subjects 1–4 (a–d, respectively). The figures on the left are the profiles for the rigid wall and those on the right are for the compliant wall. The white circle in the figures indicates the location where the maximum WSS occurs.
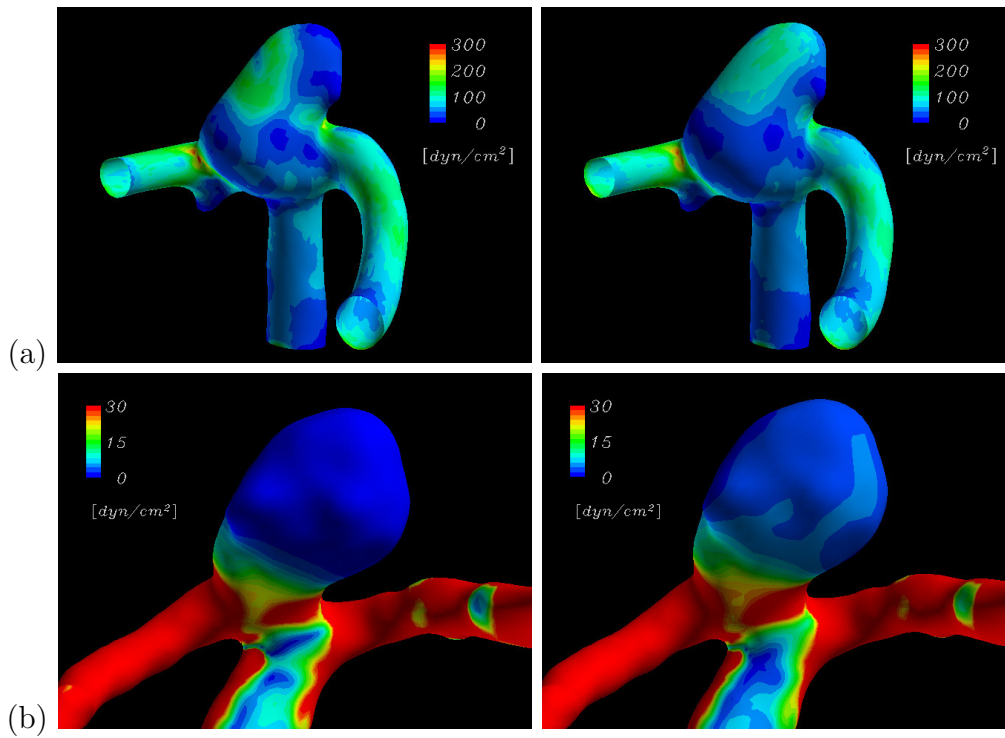
Fig. 6. Comparison of the WSS profiles (a) for Subject 2 after the peak systole (t=0.10 s) and (b) for Subject 3 at the peak systole magnified around the aneurysm. The figures on the left are the profiles for the rigid wall and those on the right are for the compliant wall.
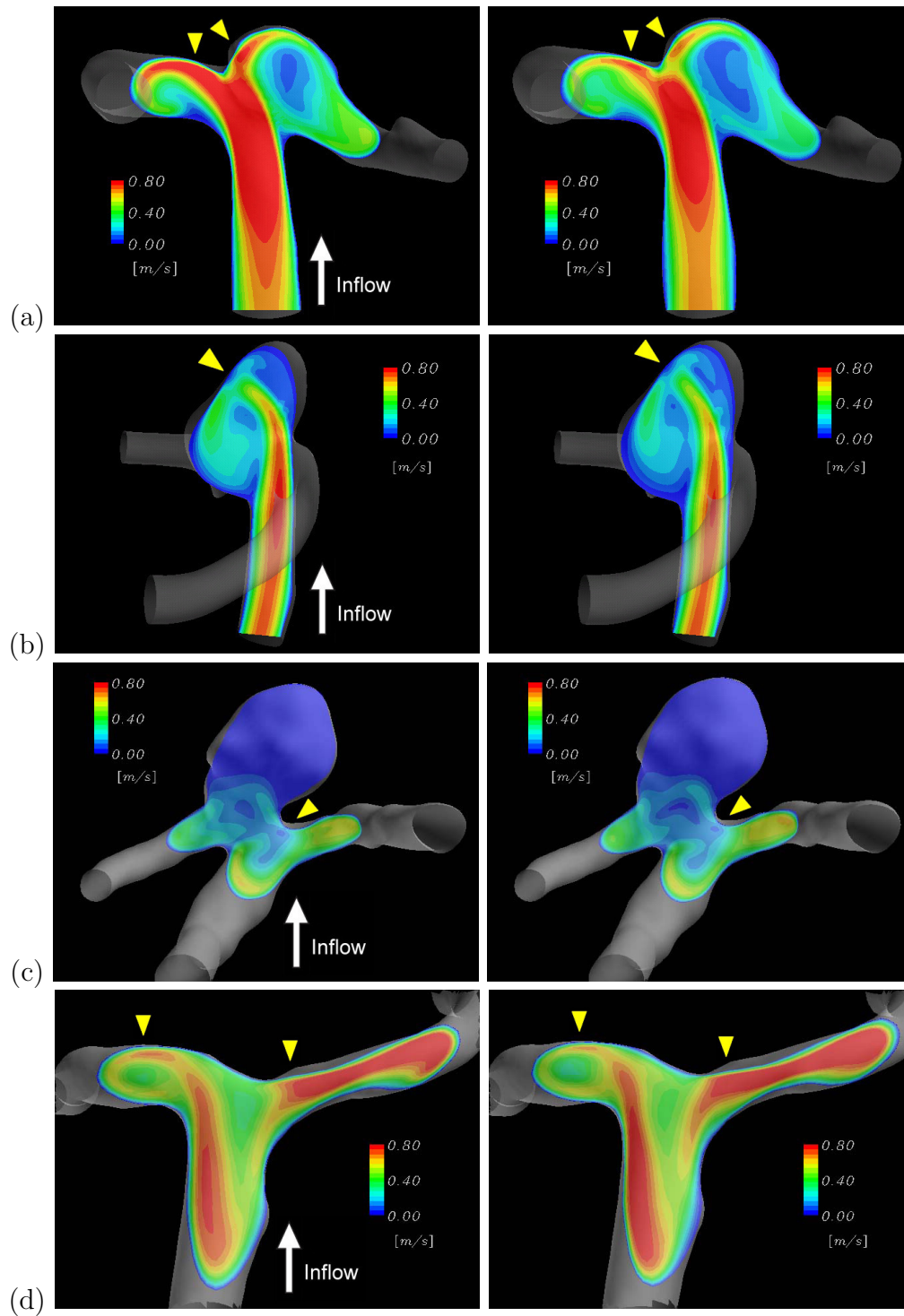
Fig. 7. Velocity profiles at a cross-section at the peak systole for Subjects 1–4 (a–d, respectively). The figures on the left are the profiles for the rigid wall and those on the right are for the compliant wall. The yellow triangles indicate the flow impingement on the wall.
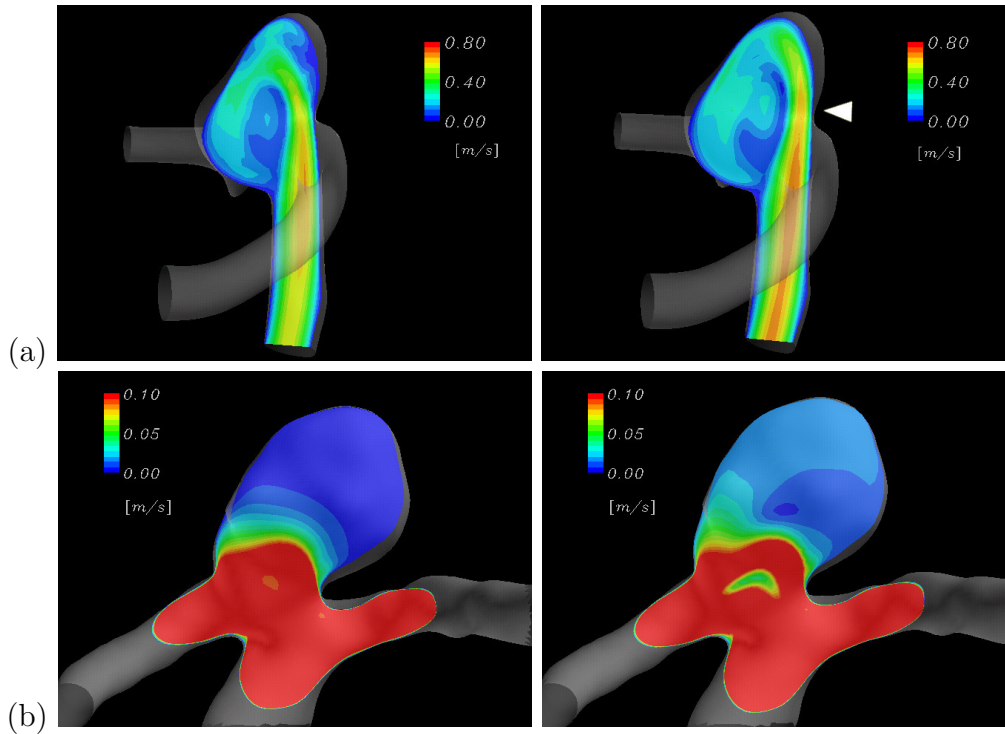
Fig. 8. Comparison of the velocity profiles at a cross-section (a) for Subject 2 after the peak systole (t=0.10 s) and (b) for Subject 3 at the peak systole with limited range of color contours to depict the slow flow region. The figures on the left are the profiles for the rigid wall and those on the right are for the compliant wall. The difference in the flow pattern owing to the displacement of the arterial wall is indicated by a white triangular marker.